

Electrical and thermal characterization of near-surface electrical discharge plasma actuation driven by radio frequency voltage at low pressure

Zhen Yang(杨臻), Hui-Min Song(宋慧敏), Di Jin(金迪), Min Jia(贾敏), Kang Wang(王康)

Citation: Chin. Phys. B . 2018, 27(8): 085205. **doi:** 10.1088/1674-1056/27/8/085205

Journal homepage: http://cpb.iphy.ac.cn; http://iopscience.iop.org/cpb

What follows is a list of articles you may be interested in

Electric ignition energy evaluation and the energy distribution structure of energy released in electrostatic discharge process

Qingming Liu(刘庆明), Jinxiang Huang(黄金香), Huige Shao(邵惠阁), Yunming Zhang(张云明)
Chin. Phys. B . 2017, 26(10): 105202. **doi:** 10.1088/1674-1056/26/10/105202

Thermal and induced flow characteristics of radio frequency surface dielectric barrier discharge plasma actuation at atmospheric pressure

Wei-long Wang(王蔚龙), Jun Li(李军), Hui-min Song(宋慧敏), Di Jin(金迪), Min Jia(贾敏), Yun Wu(吴云)
Chin. Phys. B . 2017, 26(1): 015205. **doi:** 10.1088/1674-1056/26/1/015205

Electrical and optical characteristics of the radio frequency surface dielectric barrier discharge plasma actuation

Wei-Long Wang(王蔚龙), Hui-Min Song(宋慧敏), Jun Li(李军), Min Jia(贾敏), Yun Wu(吴云), Di Jin(金迪)
Chin. Phys. B . 2016, 25(4): 045203. **doi:** 10.1088/1674-1056/25/4/045203

Conversion of an atomic to a molecular argon ion and low pressure argon relaxation

M N Stankov, A P Jovanović, V Lj Marković, S N Stamenković
Chin. Phys. B . 2016, 25(1): 015204. **doi:** 10.1088/1674-1056/25/1/015204

Current-voltage characteristics of hydrogen DC plasma torches with different sizes in an external axial magnetic field

Ma Jie, Wen Guang-Dong, Su Bao-Gen, Yang Yi-Wen, Ren Qi-Long
Chin. Phys. B . 2015, 24(6): 065205. **doi:** 10.1088/1674-1056/24/6/065205

Electrical and thermal characterization of near-surface electrical discharge plasma actuation driven by radio frequency voltage at low pressure*

Zhen Yang(杨臻), Hui-Min Song(宋慧敏)†, Di Jin(金迪), Min Jia(贾敏), and Kang Wang(王康)

Science and Technology on Plasma Dynamics Laboratory, Air Force Engineering University, Xi'an 710038, *China*

(Received 23 February 2018; revised manuscript received 11 April 2018; published online 10 July 2018)

The electrical and thermal characterization of near-surface electrical discharge plasma driven by radio frequency voltage are investigated experimentally in this paper. The influences of operating pressure, electrode distance, and duty cycle on the discharge are studied. When pressure reaches 60 Torr (1 Torr = 1.33322×10^2 Pa) the transition from diffuse glow mode to constricted mode occurs. With the operating pressure varying from 10 Torr to 60 Torr, the discharge energy calculated from the charge–voltage (Q–V) Lissajous figure decreases rapidly, while it remains unchanged between 60 Torr and 460 Torr. Under certain experimental conditions, there exists an optimized electrode distance (8 mm). As the duty cycle of applied voltage increases, the voltage–current waveforms and Q–V Lissajous figures show no distinct changes.

Keywords: radio frequency discharge, charge–voltage Lissajous figure, temperature distribution, plasma actuation

PACS: 52.80.–s, 51.50.+v, 52.50.Qt, 52.80.Vp **DOI:** 10.1088/1674-1056/27/8/085205

1. Introduction

As a novel kind of plasma aerodynamic actuation, radio frequency discharge has received increasing attention in recent years. Compared with other types of plasma discharges, radio frequency discharge has several advantages, such as better stability in high-speed air flows, higher heating efficiency, and simpler power tuning.[1–3] Leonov *et al.* found that when static pressure stays below 100 Torr the discharge mode of single-electrode radio frequency plasma is glow discharge, and as static pressure increases filamentary discharge could be observed.[4,5] Klimov *et al.* designed the surface HF plasma actuator, which is driven by 0.5-MHz high frequency AC power and 3-kV DC power. In a flow of Mach 0.4, the generated plasma consists of many filaments, and its highest gas temperature reaches about 2000 K measured by optical spectroscopy.[6] Dedrick *et al.* studied plasma propagation of surface radio frequency dielectric barrier discharge under atmospheric pressure, and the frequency was set to be 13.56 MHz. Results showed that under a lower input power, the discharge channels were not equally distributed but seemed branchlike. With the increase of input power, the distribution gradually became more uniform and the plasma channels extended further. The relationship between plasma propagation and voltage waveform was also analyzed.[7,8]

At present the measurement methods of gas discharge plasma temperature mainly include infrared thermal imager, spectroscopy, and thermocouples. Carlo *et al.* investigated the effects of actuator geometries, dielectric materials, and supply voltage on the dielectric barrier discharge (DBD) temperature. It was found that the rotational temperature obtained by spectroscopic measurements hardly changed, which is the same as the gas temperature measured by thermography.[9] Dong *et al.* evaluated the plasma temperature through spectroscopy emission at a working voltage of 8 kV and discharge frequency of 2 kHz, and the temperature rose by 40 K.[10] Joussot *et al.* investigated the thermal characteristics of DC glow discharge in a Mach 2 air flow. Experimental results showed that the surface temperature increased with the increase of current.[11] Rakshit *et al.* revealed the mechanism of dielectric surface heat transfer at several kHz. The correlation between discharge cycle and temperature distribution was analyzed experimentally, and the heat was mainly transferred from the hot air flow into the dielectric through convection.[12] Wang *et al.* measured the temperature distribution of the radio frequency DBD with an infrared thermal imager, and the influences of duty cycle, frequency, and other discharge parameters on the dielectric temperature were also analyzed.[13] The studies mentioned above mainly focus on DBD discharge, in which the discharge power is not well concentrated, and the shock control ability is quite limited, as found in the experiment.[14] With this motivation a plasma actuator with pinlike electrodes is adopted in this paper, which is believed to be promising in power concentration and subsequently enhancing the effect of shock wave control.

Low pressure is a typical environment for aircraft, which has great influences on the plasma characteristics and flow control effect.[15,16] Liu *et al.* found that a transition between the striated and non-striated modes for capacitively coupled ra-

*Project supported by the National Natural Science Foundation of China (Grant Nos. 11472306, 51407197, and 51507187).

†Corresponding author. E-mail: min_cargi@sina.com

© 2018 Chinese Physical Society and IOP Publishing Ltd

dio frequency CF4 plasmas can be observed by changing the pressure.[17] Therefore, the influences of operating pressure, as well as electrode distance, and duty cycle on the electrical and thermal characteristics of radio frequency discharge are investigated experimentally.

2. Experimental setup

Figure 1(a) shows the schematic diagram of the experimental setup which includes a radio frequency generator/amplifier, a plasma actuator, and diagnosis system. The plasma actuator is powered by radio frequency generator/amplifier (AG 1017L, T & C). The operating frequency can be adjusted from 10 kHz to 10 MHz, and the maximum output power can reach 500 W. When working in the internal pulse mode, the restart period is 1 ms–50 ms and the burst width is 1 μs–500 μs. As shown in Fig. 1(b), the plasma actuation is generated between two tungsten pinlike electrodes each with a diameter of 2 mm, which are flush-mounted on an alumina ceramic plate (80 mm×30 mm×10 mm). Three different electrode gaps (6 mm, 8 mm, and 10 mm) are designed. During the experiment the plasma actuator is placed in a pressure chamber and fixed 30 mm away from the optical window. What is more, an impedance matching circuit between the radio frequency generator/amplifier and the plasma actuator are used to adequately couple the power.

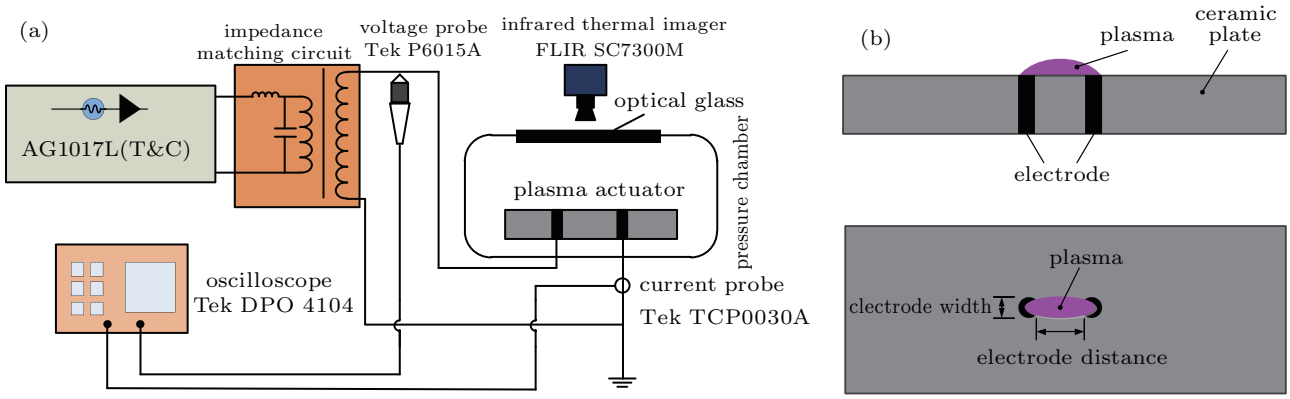


Fig. 1. (color online) Schematic diagrams of the experimental setup and plasma actuator.

The digital oscilloscope (Tektronix DPO4104) together with a high voltage probe (Tektronix P6015 A) and a current probe (Tektronix TCP0030 A) are used to collect and store the voltagecurrent plots. The surface temperature measurements are carried out using an FLIR SC7300M Infrared Thermal Imager with a spectral range of 3.7 μm–4.8 μm and an MCT IR photo-detector composed of a 320 × 240-pixel array. The temperature between −20 °C and 1500 °C could be measured.

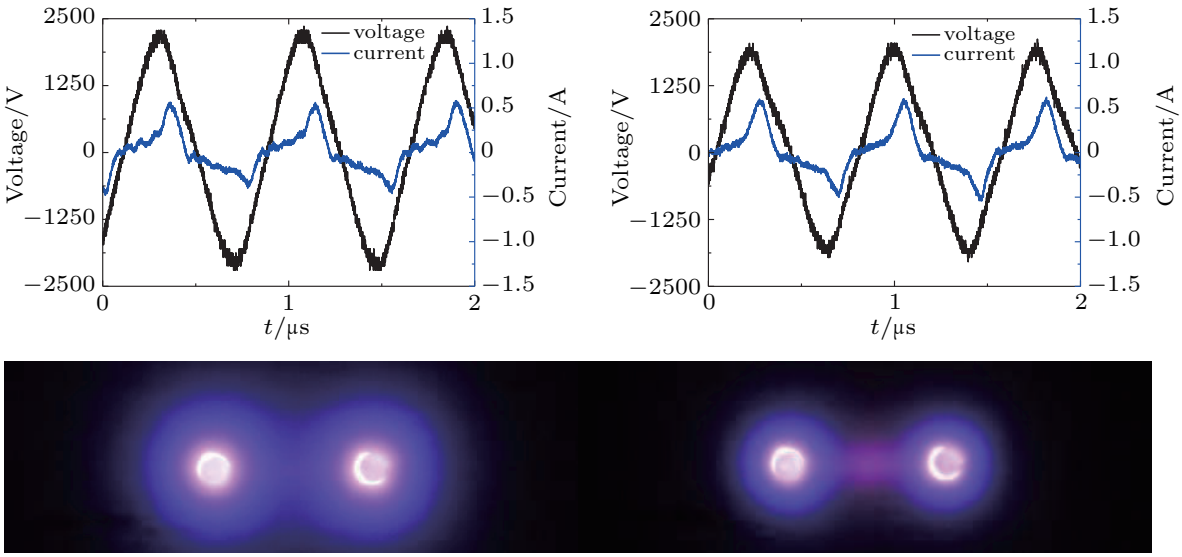
3. Results and discussion

3.1. Electrical characteristics

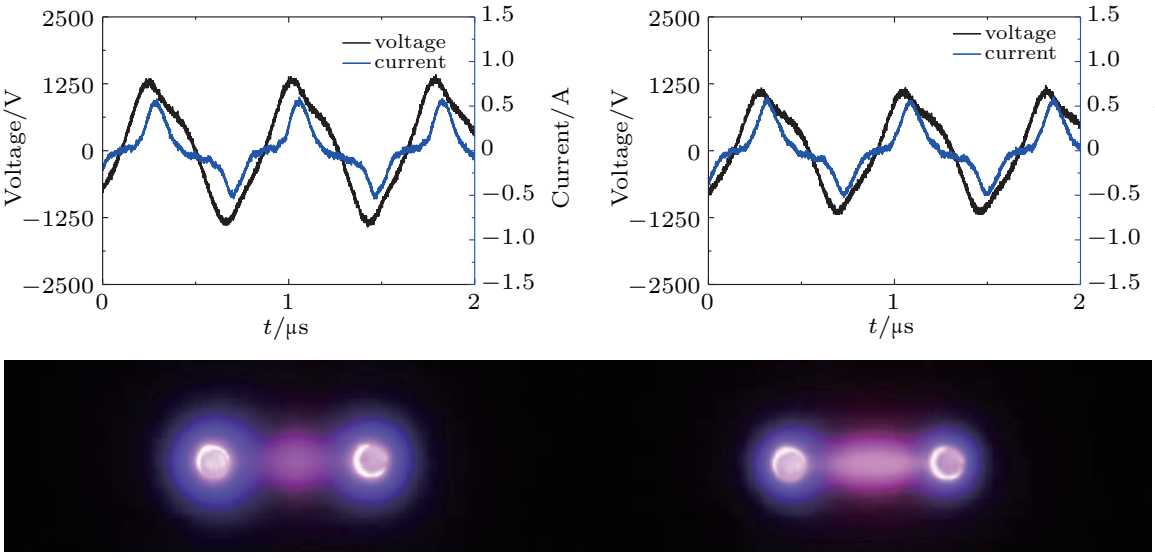
The influences of operating pressure, electrode distance, and duty cycle on the voltagecurrent waveforms and discharge mode are investigated experimentally, and the relationship between the energy per cycle and the impedance magnitude is discussed based on *Q*–*V* Lissajous figures.

3.1.1. Influence of operating pressure on electrical characteristics

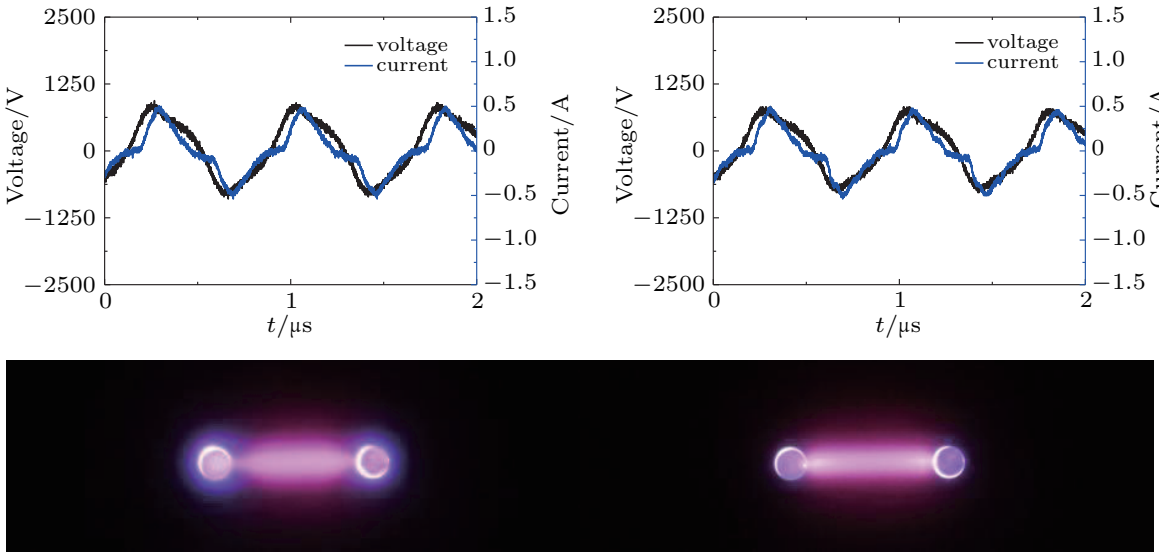
Figure 2 shows the voltagecurrent waveforms and discharge images under different operating pressures (10 Torr–460 Torr). The experimental conditions are shown in Table 1. A phase difference between the voltage and current waveforms is observed due to the non-resistively coupled system. Since two electrodes of the actuator are exactly identical, self-bias on the electrodes can be considered as zero and as a result the voltage waveforms are symmetrical in the positive and negative half-cycles. For the operating pressures of 10 Torr and 20 Torr, the voltage plots are smooth continuous sine waves, and the current waveforms exhibit a distinct single peak every half cycle. What is more, there exists a diffuse luminous discharge around the electrodes, which can be categorized into diffuse glow discharge mode. With operating pressure varying from 30 Torr to 460 Torr, the voltage waveform is distorted near the current peak. At the same time, a luminous discharge channel between electrodes gradually forms. However, the peak current is much smaller than that of the typical arc discharge, indicating that it is just a constricted arc-like discharge but not real thermal arc. From the above analysis it can be inferred that the operating pressure plays an important role in generating the radio frequency discharge plasma. In fact as operating pressure increases and the mean-free-path decreases, the characteristic dimension of the discharge decreases and the spatial extent of the plasma region decreases correspondingly. As a result, the transition from diffuse discharge mode to constricted discharge mode occurs.[18,19] It needs to be added that when the pressure is higher than 260 Torr, the discharge channel begins to shake unsteadily, indicating that the discharge is more and more difficult to maintain. After 580 Torr, the discharge channel goes out completely.



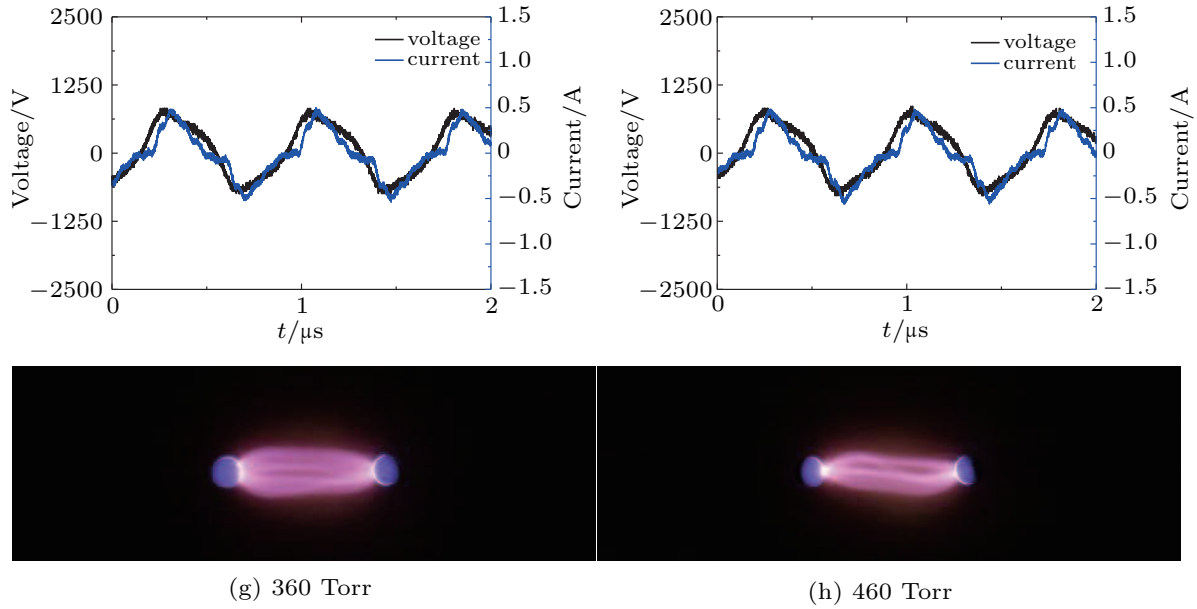
(a) 10 Torr (b) 20 Torr



(c) 30 Torr (d) 60 Torr



(e) 100 Torr (f) 260 Torr



(g) 360 Torr (h) 460 Torr

Fig. 2. (color online) Voltage–current waveforms and discharge images versus operating pressure.

Table 1. Experimental conditions for the first series of experiments.

Parameter	Value
Output power/W	100
Frequency/MHz	1.30
Duty cycle/%	20
Electrode distance/mm	10

The general electrical parameters such as peak voltage, transported charge, etc. can be deduced from Q–V Lissajous figures. The area of figure represents the energy per cycle,[20] which can be calculated from

$$E = \int Q \cdot \mathrm{d}V = A_{\mathrm{Lissajous}}. \tag{1}$$

Obviously, the electrical characteristics can be further analyzed from the Lissajous figures. Under different operating pressures the Q–V Lissajous figures all present the quasi-parallelogram shapes shown in Fig. 3. For the near-surface electrical discharge the slope of the left and right side of the figure are both negative, which is different from the scenario of radio frequency DBD.[21] This is mainly because the current phase lags behind the voltage phase. The largest area of Q–V Lissajous figure is acquired at a pressure of 10 Torr. When the operating pressure changes from 6 Torr to 10 Torr, the area of the figure as well as the corresponding slope gradually decreases, and the area hardly changes when the pressure is higher than 60 Torr.

Based on the Q–V Lissajous figure, the variation of energy per cycle can be concluded as shown in Fig. 4(a). When operating pressure varies from 10 Torr to 60 Torr, the energy per cycle decreases from 0.21 mJ to 0.08 mJ, whereas the energy per cycle remains unchanged at about 0.08 mJ when operating pressure is higher than 60 Torr. In fact, it has been confirmed that the energy per cycle is closely related to the impedance magnitude according to the study of the DBD electrical characteristics.[22] When the actual impedance magnitude of the actuator, calculated by the voltage and current waveform, is closer to its optimal value, the discharge energy coupled into the actuator is larger. Therefore, the influence of operating pressure on the Q–V Lissajous figure mainly lies in the change of the impedance magnitude of the actuator. The above analysis of the discharge mode shows that with the operating pressure increasing to 60 Torr the transition from glow discharge to the arc-like discharge occurs and the tendency of the impedance magnitude also changes. The variation of impedance magnitude with operating pressure in Fig. 4(b) is also consistent with the above analysis.

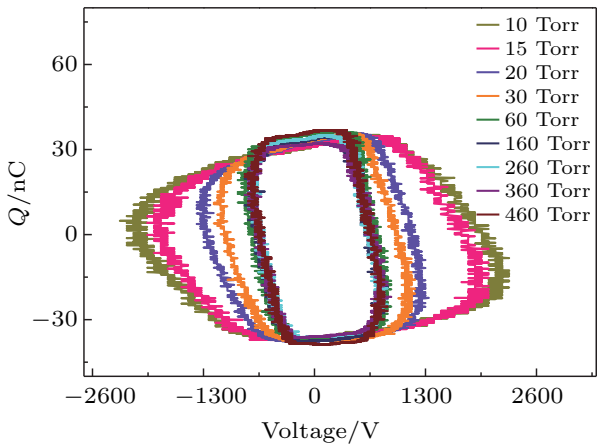


Fig. 3. (color online) Q–V Lissajous figures versus operating pressure.

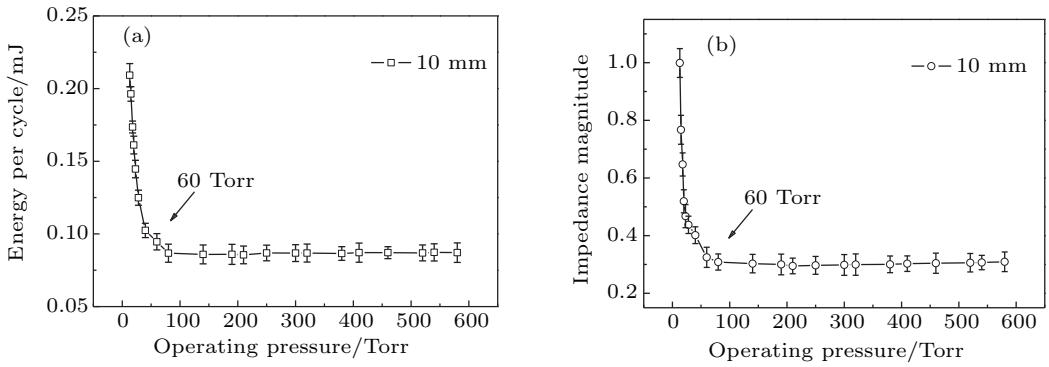


Fig. 4. (a) Energy per cycle and (b) impedance magnitude versus operating pressure.

3.1.2. Influence of electrode distance on electrical characteristics

Electrode distance, as an important geometrical parameter, is closely related to the breakdown voltage and the impedance magnitude of the actuator. The experimental conditions are shown in Table 2. From Fig. 5 the constricted arc-shaped discharge can be observed, and the shape of the voltage–current waveform shows little difference. When electrode distance is 6 mm, the peak voltage is less than that of 8 mm and 10 mm, indicating that the discharge of 6 mm is easiest. The peak current of 6 mm is the largest in those peak currents of three distances.

Subsequently, the *Q*–*V* Lissajous figures of different electrode distances are obtained when discharge power varies from 40 W to 80 W. As shown in Figs. 6(a)–6(c), for a fixed distance, the area of the figures gradually increases with the rise of the power, but the slope of each side remains the same. For a fixed power, the shapes of *Q*–*V* Lissajous figures are different with different electrode distances.

Table 2. Experimental conditions for the second series of experiments.

Parameter	Value
Output power/W	95
Frequency/MHz	1.30
Operating pressure/Torr	40
Duty cycle/%	20

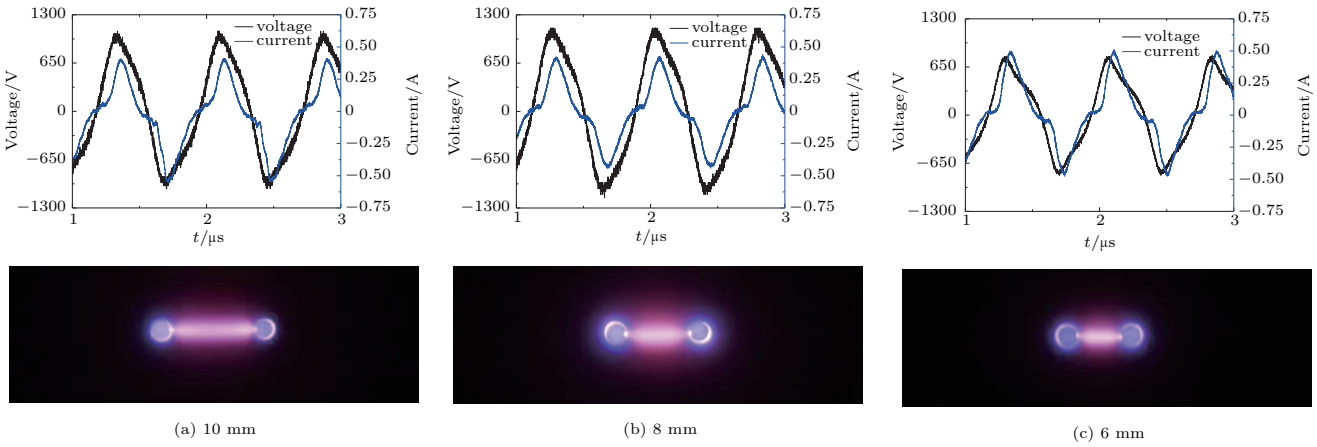


Fig. 5. (color online) Voltage–current waveforms and discharge images versus electrode distance.

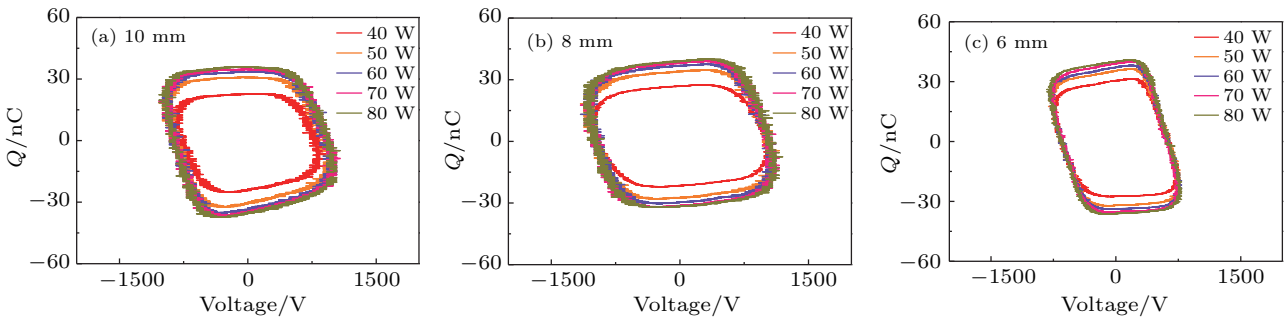


Fig. 6. (color online) *Q*–*V* Lissajous figures of radio frequency discharge versus electrode distance.

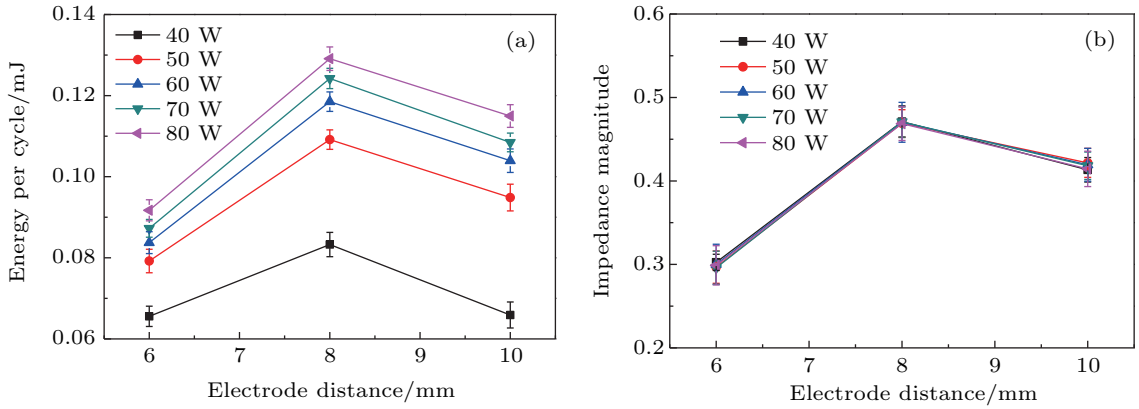


Fig. 7. (color online) Variations of (a) energy per cycle and (b) impedance magnitude with electrode distance.

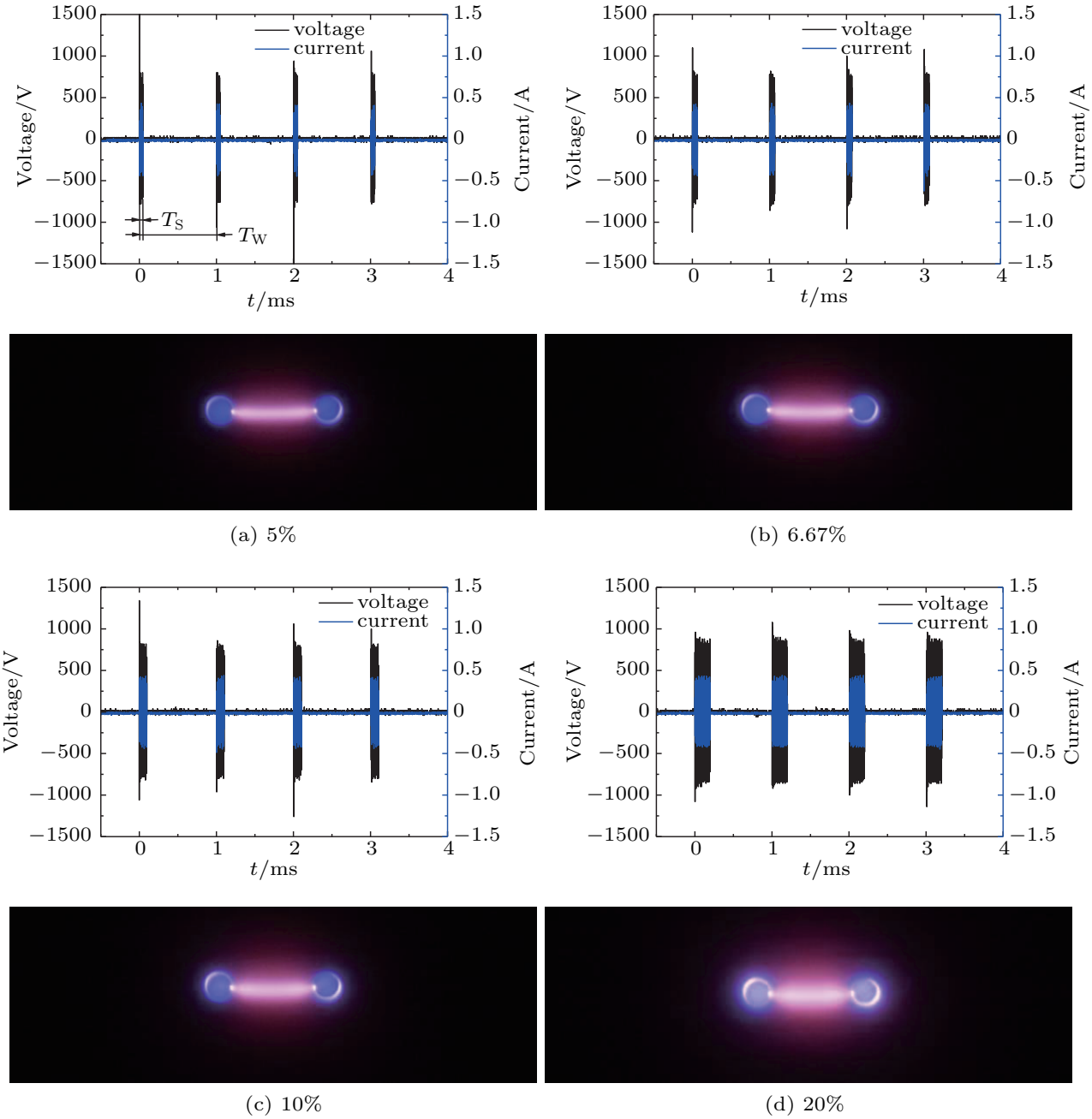


Fig. 8. (color online) Voltage–current waveforms and discharge images with different duty cycles.

From Fig. 7 it can be seen that the energy per cycle, calculated from the Q–V Lissajous figures, is the largest for the electrode distance of 8 mm while it is the smallest for 6 mm. For a fixed power the larger the energy per cycle, the larger the impedance magnitude will be. It can be inferred that there exists an optimized electrode distance where the best impedance matching can be achieved to acquire the largest energy per cycle. What is more, for a fixed electrode distance different powers correspond to the only impedance magnitude, indicating that the power does not have an influence on the impedance magnitude when the discharge mode keeps unchanged.

3.1.3. Influence of duty cycle on electrical characteristics

The T_S/T_W is defined as the duty cycle, where T_S is the burst width, and T_W is the restart period. Figure 8 shows the voltage–current waveforms and discharge images with different duty cycles. The experimental conditions are shown in Table 3. With the increase of duty cycle, no significant change in the peak voltage or peak current can be observed, while burst width T_S gradually increases. Besides, with duty cycle increasing the luminosity and width of discharge channels also increase significantly, indicating a stronger discharge.

Table 3. Experimental conditions for the third series of the experiments.

Parameter	Value
Output power/W	90
Frequency/MHz	1.30
Operating pressure/Torr	50
Electrode distance/mm	8

As can be seen from Figs. 9 and 10, with the increase of duty cycle, Q–V Lissajous figures exhibit almost no change, and the corresponding energy per cycle is basically the same, so is the impedance magnitude. Actually in the pulse mode the adjustment of duty cycle only changes the burst width, but the discharge waveform per cycle is hardly influenced. Therefore, none of the shapes of Q–V Lissajous figures, the energy per cycle, and the impedance magnitude are changed.[22]

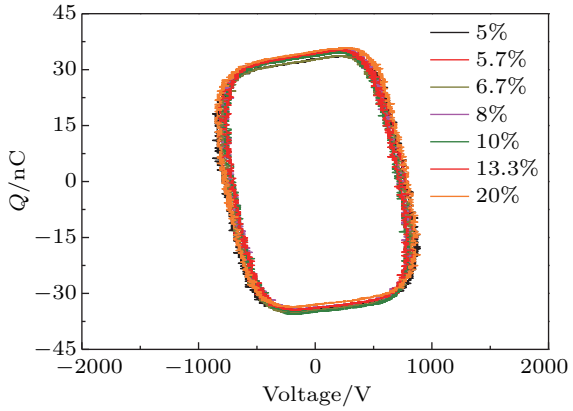


Fig. 9. (color online) Q–V Lissajous figures versus duty cycle.

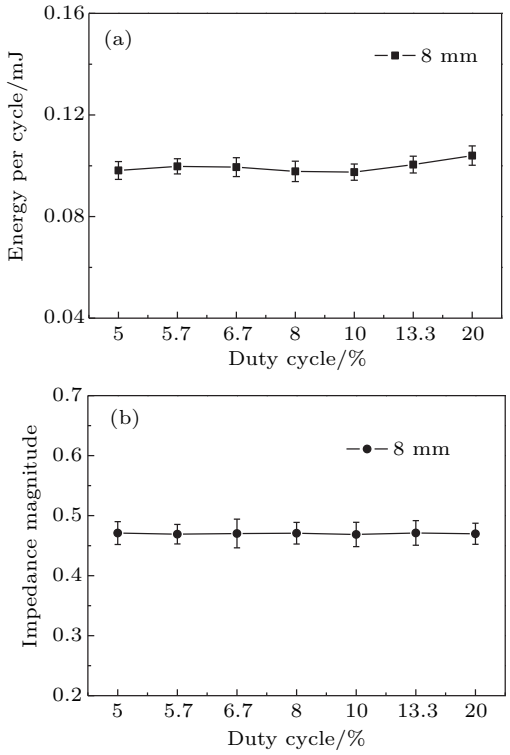


Fig. 10. (a) Energy per cycle and (b) impedance magnitude versus duty cycle.

3.2. Thermal characteristics

In this subsection, the spatiotemporal distribution of the radio frequency discharge plasma temperature at low pressure is investigated, and the effects of operating pressure, electrode distance, and duty cycle on the thermal characteristics are analyzed.

3.2.1. Spatiotemporal distribution of surface temperature at low pressure

For each experimental case, the temperature measurement is not performed until the thermal equilibrium is reached among plasma, actuator, and surrounding air. In addition, the distance between the actuator and the thermal imager is only 30 mm, indicating that the heat absorbed by the water vapor and carbon dioxide is negligible. What is more, the temperature measured by the thermal imager (T_c) and the actual temperature of the actuator surface (T_o) are not strictly equal, and the relationship between them is expressed as follows:[11,24]

$$T_c^4 = \varepsilon_o T_o^4 + (1-\varepsilon_o) T_a^4, \tag{2}$$

where ε_o is the emissivity of the actuator and T_a is the room temperature. Then the surface temperature of the actuator can be deduced as

$$T_o = \sqrt[4]{\frac{T_c^4 - (1-\varepsilon_o) T_a^4}{\varepsilon_o}}. \tag{3}$$

In the experiment, the room temperature T_a is 30 °C, the emissivity of the ceramic plate ε_o is 0.94, and the germanium glass with a transmission rate of 0.43 is installed in the optical window.

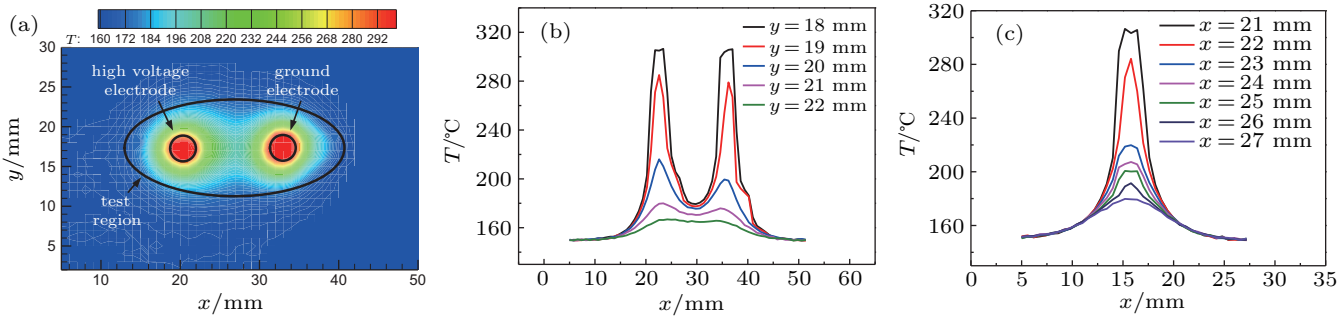


Fig. 11. (color online) (a) Thermogram of actuator surface temperature recorded by thermal imager, (b) variations of surface temperature along (b) transversal direction and (c) longitudinal direction.

Table 4. Experimental conditions for the fourth series of the experiments.

Parameter	Value
Output power/W	86
Frequency/MHz	1.30
Operating pressure/Torr	50
Duty cycle/%	13.3
Electrode distance/mm	6

Based on the above analysis the temperature spatial distribution on the actuator surface can be obtained as shown in Fig. 11. The experimental conditions are shown in Table 4. As shown in Fig. 11(a), the high voltage and the grounded electrode are represented by the black circle. It can be observed that the high temperature region covers the entire electrodes and the area around. Figure 11(b) displays the evolutions of the surface temperature along the transversal direction (x axis) at different ordinate values ($y = 18$ nm–22 mm). Figure 11(c) indicates the evolutions of the surface temperature along the longitudinal direction (y axis) at different abscissa values ($x = 21$ mm–27 mm). From Figs. 11(b) and 11(c) for each curve the highest temperature (more than 300 °C) appears inside the electrodes, then it gradually reduces away from the electrodes.

Since the voltage waveforms are symmetrical in the positive and negative half-cycles, the accumulation of the discharge energies converted into heat on the high voltage and ground electrode can be considered as equal, leading the temperatures of the two electrodes to be almost the same, which is quite different from the scenario in DC glow discharge where the cathode surface is hottest.[25]

In the above thermogram the high temperature region is concentrated near the electrodes, therefore the average temperature of the elliptical area shown in Fig. 11(a) is analyzed. Figure 12 shows the average temperature at different frequencies (0.46 MHz–1.30 MHz). At the beginning of the discharge, the surface temperature rises rapidly, and then its slope gradually decreases. At 150 s the thermal equilibrium is achieved among plasma, actuator, and air. Because of heat convection induced temperature fluctuation, several spikes can be found from each curve. In addition, the surface temperature of the actuator always ascends with the increase of the power frequency.

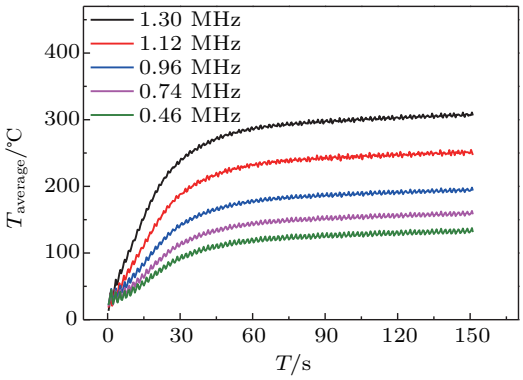


Fig. 12. (color online) Evolutions of the surface temperature with time.

3.2.2. Influence of operating pressure on thermal characteristics

The thermograms of the radio frequency discharge under different pressures (10 Torr–460 Torr) are shown in Fig. 13. The experimental conditions are shown in Table 1. When the pressure is under 30 Torr, the high temperature region is mainly concentrated on the electrode surface, corresponding to the diffused glow discharge. As the operating pressure increases from 30 Torr to 60 Torr, the high temperature around the electrode surface gradually decreases. Conversely, the temperature of the discharge channel between the electrodes increases as a result of the transition from diffuse glow mode to constricted mode. Under the operating pressure higher than 60 Torr the fall of the discharge channel temperature occurs while the temperature on the electrode surface is always the highest. Results show that the temperature distribution of the plasma actuator is in accordance with the scenario for its discharge mode.

It can be observed that different operating pressures correspond to different surface temperatures of the actuator. Obviously, the main factor determining the surface temperature is the discharge energy converted into heat. The calculation formula of the discharge energy can be approached to the following expression:

$$\text{Energy}_{\text{heat}} = \eta \text{Energy}_{\text{cycle}} \frac{T_{\text{S}}}{T_{\text{W}}} \Delta T, \tag{4}$$

where $\text{Energy}_{\text{heat}}$ is the discharge energy converted into heat, $\text{Energy}_{\text{cycle}}$ is the energy per cycle, ΔT is the heating time, η is the heating efficiency, and $T_{\text{S}}/T_{\text{W}}$ is the duty cycle. Keeping other conditions unchanged the operating pressure is related to the energy per cycle $\text{Energy}_{\text{heat}}$ and the heating efficiency η. The variations of the energy per cycle under different operating pressures are obtained as indicated in Fig. 3(b). Also in the experiment it is found that when the operating pressure is higher than 260 Torr the heating efficiency η gradually decreases due to the discharge instability.

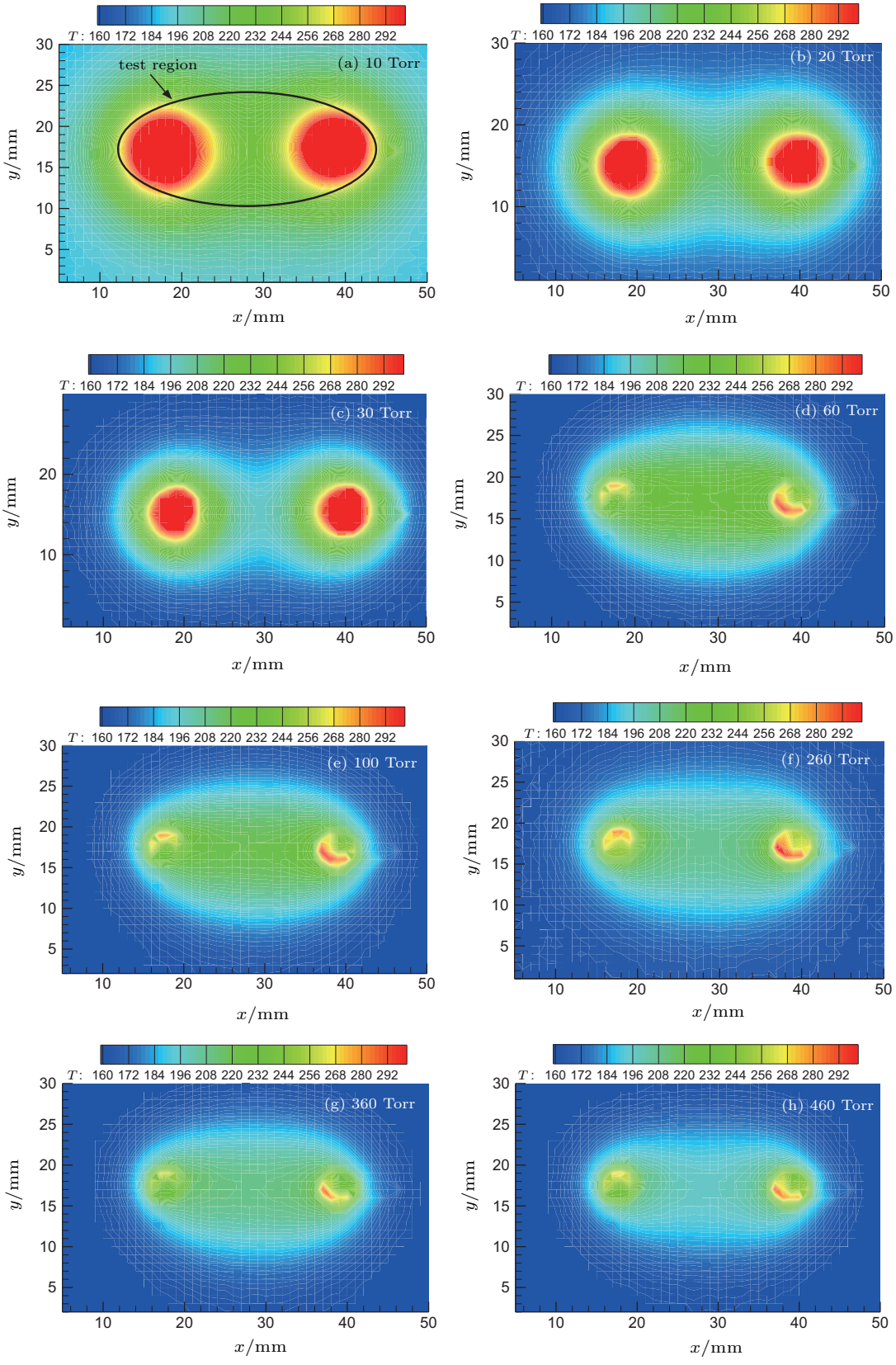


Fig. 13. (color online) Thermographs of surface temperature versus operating pressure at different pressures.

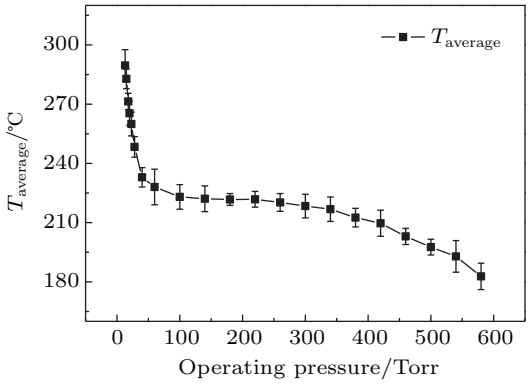


Fig. 14. Average temperature versus operating pressure.

Both of them affect the accumulation of discharge energy together. According to the variation of the surface temperature shown in Fig. 14, it can be explained that when the operating pressure is lower than 60 Torr the average temperature gradually decreases, and then it remains almost unchanged with operating pressure varying from 60 Torr to 260 Torr. Obviously these trends of the temperature variation are related to the energy per cycle under different operating pressures. When the operating pressure goes up more than 260 Torr, the surface temperature begins to decrease gradually, indicating that the decrease of the heating efficiency becomes the main factor.

3.2.3. Influence of electrode distance on thermal characteristics

Figure 15 shows the thermograms of the surface temperature at different electrode distances. The experimental conditions are shown in Table 2. It can be found that all the high temperature regions are spindly, corresponding to the constricted discharge mode. As the electrode distance increases, the high temperature regions gradually extend.

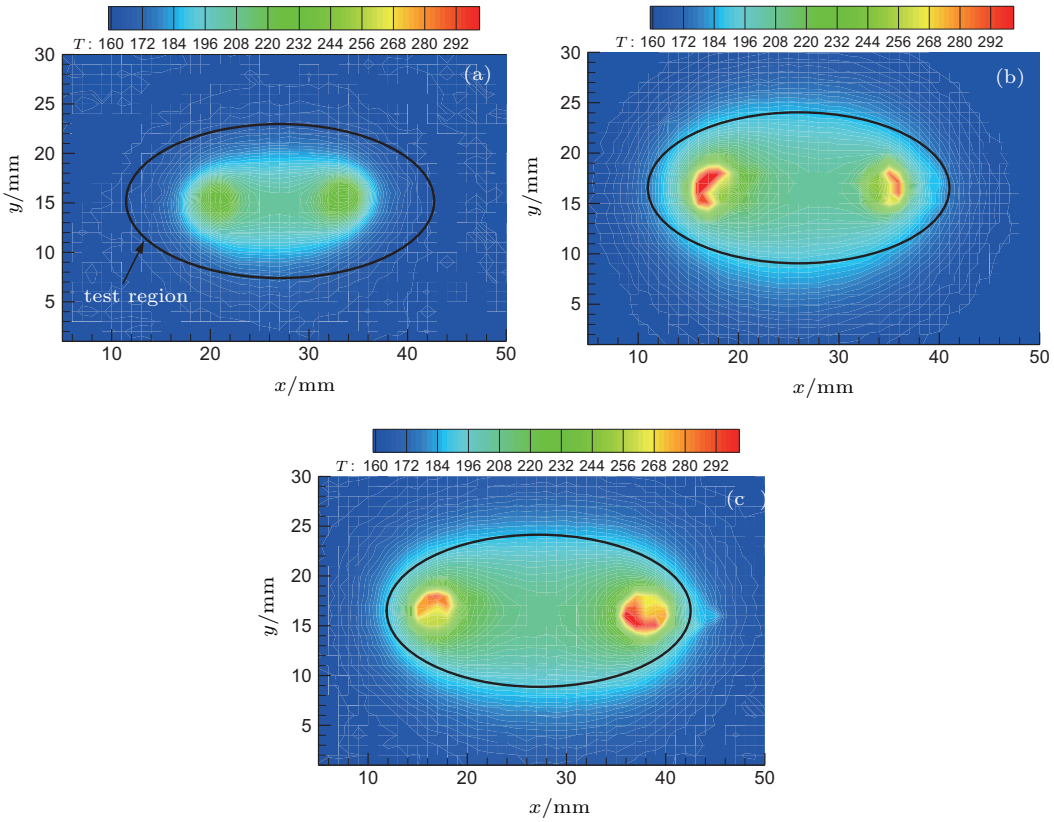


Fig. 15. (color online) Thermographs of surface temperature varying with x under varying electrode distances: (a) 6 nm, (b) 8 nm, and (c) 10 nm.

From Fig. 16 it can be seen that the highest average temperature is acquired when the electrode distance is 8 mm, while the lowest value is observed with the electrode distance being 6 mm. In the case of 8 mm, the largest discharge energy per cycle is achieved, which leads to a stronger heating effect.

3.2.4. Influence of duty cycle on thermal characteristics

This subsection focuses on the effect of duty cycle on the surface temperature. The experimental conditions are shown in Table 3. As shown in Fig. 17, the high temperature regions are mainly concentrated near the electrodes and the discharge path between the electrodes. As the duty cycle increases, the surface temperature gradually increases, and the high temperature region gradually expands. For a larger duty cycle the burst width becomes longer, which means that more heat can be deposited. As a result the temperature will be higher, and it agrees well with that found in radio frequency DBD discharge.[13]

From formula (4) it can be concluded that keeping other conditions unchanged, with the duty cycle increasing the discharge energy increases, thus the average temperature increases linearly. As shown in Fig. 18, the average surface temperature evolves with the duty cycle as

$$y = a + bx, \tag{5}$$

where $a = 184.30 \pm 0.78$ and $b = 397.36 \pm 9.19$ are best-fit values with the determination coefficient $r^2 = 0.9994$. Due to the determination coefficient being close to one, the experimental variation of the surface temperature shows good agreement with the theoretical trend.

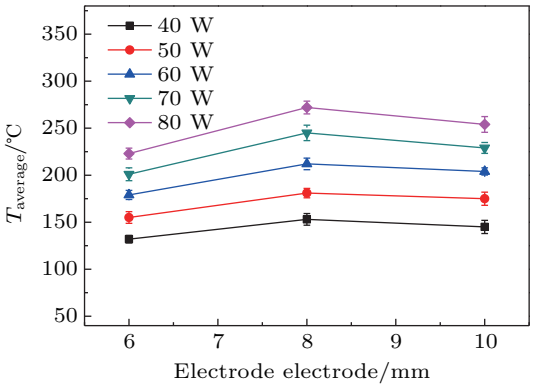


Fig. 16. (color online) Average temperatures versus electrode distance at different powers.

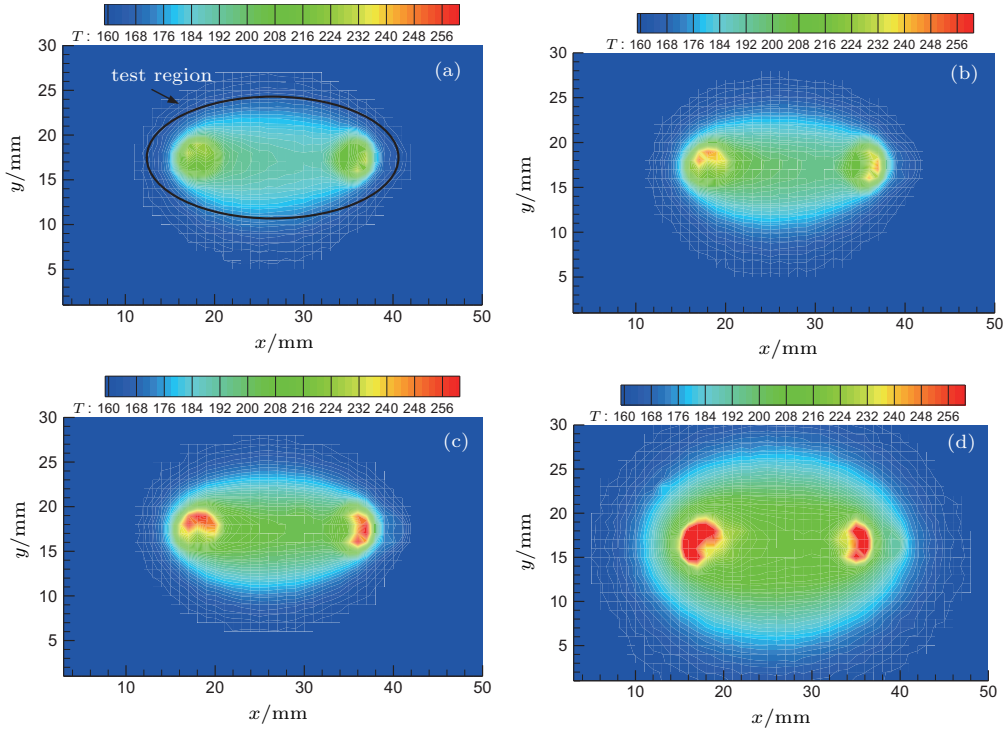


Fig. 17. (color online) Thermographs of surface temperature versus duty cycle at different duty cycles: (a) 5%, (b) 6.7%, (c) 10%, and (d) 20%.

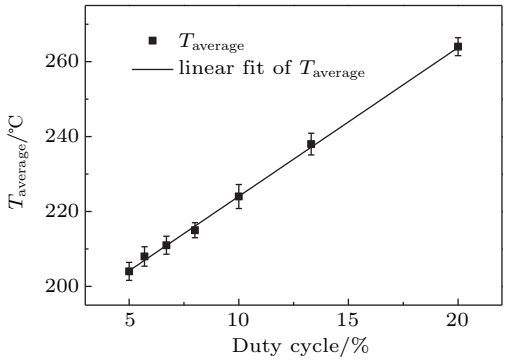


Fig. 18. Average temperature versus duty cycle.

4. Conclusions

The characteristics of near-surface electrical discharge plasma actuation driven by radio frequency voltage are experimentally investigated, and the influences of some parameters, such as operating pressure, electrode distance, and duty cycle are discussed. The main conclusions are as follows.

A phase difference between discharge voltage and current is observed, which is typical of a non-resistively coupled system. When the operating pressure is between 10 Torr and 20 Torr, the voltage waveforms are smooth continuous sine waves, and an obvious single peak pattern is shown in each half cycle for the current waveform. A diffuse luminous discharge is clearly visible around the electrodes, from which a diffuse glow discharge mode can be deduced. With operating pressure varying from 30 Torr to 460 Torr, a luminous discharge channel appears between two electrodes, and the voltage waveform is distorted near the current peak. Under different operating pressures, the shapes of *Q*–*V* Lissajous figures are quasi-parallelogram, and the slopes of both left and right sides are negative due to the voltage phase being ahead

of the current phase. Under the given conditions, at 10 Torr the area of the Q–V Lissajous figure is biggest. When operating pressure ascends from 10 Torr to 60 Torr, the area gradually decreases, so does the corresponding slope. At pressure higher than 60 Torr, the change of the area is negligible.

For a fixed electrode distance, the area of the Lissajous figure gradually increases with the increase of discharge power. For a fixed power, the shape of the Q–V Lissajous figure varies with electrode distance. The area of Q–V Lissajous figure corresponding to the electrode distance of 8 mm is largest, while the area for 6 mm is smallest. For certain experimental parameters, an optimal electrode distance exists, thereby the best impedance matching between actuator and radio frequency power supply can be achieved.

The duty cycle has little influence on the voltage–current waveform, QV Lissajous figure, and energy per cycle, while the discharge intensity increases as duty cycle rises.

The temperature of the high voltage electrode and the ground electrode are almost equal, which is different from the result of DC glow discharge. The surface temperature of the plasma actuator rises rapidly after breakdown, and then the rising rate gradually decreases. Approximately 150 s after discharge, thermal equilibrium is achieved among plasma, actuator, and air.

Under lower pressure, the high temperature region is concentrated on the electrode surface. As operating pressure increases, the high temperature region turns to be evidently spindly. The average temperature corresponding to the electrode distance of 8 mm is highest, while it is lowest when the electrode distance is 6 mm. With the increase of duty cycle, the average temperature basically increases linearly, and the high temperature region also increases gradually.

For the purpose of improving the aerodynamic control efficiency for the shock wave with supersonic flow, the future work should focus on the influence of supersonic flow on the characteristics of radio frequency discharge. What is more, based on the study of the characteristics the control of the shock strength and drag by radio frequency discharge actuation in wind tunnel experiments will also be investigated.

References

[1] Jaeyoung Park, Henins I, Herrmann H W, Selwyn G S and Hicks R F 2001 *J. Appl. Phys.* **89** 20

[2] Wu Yun and Li Yinghong 2015 *Hangkong Xuebao/acta Aeronautica Astronautica Sin.* **36** 381

[3] Smith H B, Charles C and Boswell R W 2003 *Phys. Plasmas* **10** 875

[4] Leonov S, Bityurin Valentin and Kolesnichenko Y 2001 39*th AIAA Aerosp. Sci. Meeting & Exhibit*, 8–11 January, 2001, Reno, USA, **111** 12620

[5] Leonov S and Yarantsev D A 2008 *J. Propul. Power* **24** 1168

[6] Klimov A, Bitiurin V, Moralev I, Tolkunov B, Zhirnov K and Kutlaliev V 2008 46*th AIAA Aerosp. Sci. Meeting Exhibit*, 7–10 January, 2008, Reno, USA, p. 1386

[7] Dedrick J, Boswell R W, Audier P, Rabat H, Hong D and Charles C 2011 *J. Phys. D: Appl. Phys.* **44** 205202

[8] Dedrick J, Boswell R W, Rabat H, Hong D and Charles C 2012 *Plasma Sources Sci. Technol.* **21** 055016

[9] Borghi A, Andrea Cristofolini, Chiara Latini and Gabriele Neretti 2010 41*st Plasmadynamics and Lasers Conference*, June 28–July 1, 2010, Chicago, USA, p. 4763

[10] Dong B, Bauchire J M, Pouvesle J M, Magnier P and Hong D 2008 *J. Phys. D: Appl. Phys.* **41** 155201

[11] Joussot Romain, Lago Viviana, Parisse Jean Denis 2015 *Exp. Fluids* **56** 102

[12] Rakshit Tirumala, Nicolas Benard, Eric Moreau, Matthieu Fenot, Gildas Lalizel and Eva Dorignac 2014 *J. Phys. D: Appl. Phys.* **47** 255203

[13] Wang W L, Song H M, Li J, Jin D, Jia M and Wu Y 2017 *Chin. Phys. B* **26** 015205

[14] Wang W L, Song H M, Li J, Jin D, Jia M and Wu Y 2017 21*st AIAA Int. Space Planes Hypersonics Technol. Conference*, 6–9 March, 2017, Xiamen, China, p. 2283

[15] Song H M, Jia M, Jin D, Cui W and Wu Y 2016 *Chin. Phys. B* **25** 035204

[16] Gao L, Zhang B L, Li Y W, Duan C D and Wang Y T 2016 *Plasma Sci. Technol.* **18** 855

[17] Liu Y X, Ihor Korolov, Edmund Schungel, Wang Y N, Žoltan Donkó and Julian Schulze 2017 *Phys. Plasmas* **24** 275001

[18] Jichul Shin 2007 "A Study Direct-Curr. Surf. Discharge Plasma For A Mach 3 supersonic flow control" Ph. D. Dissertation (The University of Texas at Austin)

[19] Jichul Shin, Narayanaswamy V, Raja L and Clemens T 2007 *AIAA J.* **45** 1596

[20] Jiang Hui, Shao Tao, Zhang Cheng, Li Wenfeng, Yan Ping 2013 *IEEE Trans. Dielectrics Electr. Insulation* **20** 1101

[21] Zhang Yu Tao 2007 "A study on improving the homogeneity and stability of atmospheric pressure air plasma", Ph. D. Dissertation (Dalian: Dalian University of Technology) (in Chinese)

[22] Wang W L, Song H M, Li J, Jia M, Wu Y and Jin D 2016 *Chin. Phys. B* **25** 045203

[23] Léger L, Depussay E and Lago V 2009 *IEEE Trans. Dielectrics Electr. Insulation* **16** 396

[24] Joussot R, Hong D, Rabat H, Boucinha V, Weber-Rozenbaum R and Leroy-Chesneau A 2010 40*th AIAA Fluid Dyn. Conference Exhibit*, 28 June–1 July, 2010, Chicago, USA, p. 5102

[25] Stanfield A, James Menart, Joseph Shang, Kimmel L and Hayes R 2006 44*th AIAA Aerosp. Sci. Meeting Exhibit*, 9–12 January, 2006, Reno, USA, p. 0559